Engineering 18 (2022) 232–245

Contents lists available at ScienceDirect

Engineering

journal homepage: www.elsevier.com/locate/eng

Research
Civil Engineering Materials—Article

Tailoring Anti-Impact Properties of Ultra-High Performance Concrete by Incorporating Functionalized Carbon Nanotubes

Jialiang Wang [a], Sufen Dong [b,*], Sze Dai Pang [c], Xun Yu [d], Baoguo Han [a,*], Jinping Ou [a]

[a] School of Civil Engineering, Dalian University of Technology, Dalian 116024, China
[b] School of Transportation and Logistics, Dalian University of Technology, Dalian 116024, China
[c] Department of Civil and Environmental Engineering, National University of Singapore, Singapore 117576, Singapore
[d] Department of Mechanical Engineering, New York Institute of Technology, New York, NY 11568, USA

ARTICLE INFO

Article history:
Received 19 October 2020
Revised 3 March 2021
Accepted 6 April 2021
Available online 26 October 2021

Keywords:
Functionalized carbon nanotubes
Concrete
Anti-impact properties
Reinforcing mechanisms

ABSTRACT

Replacing micro-reinforcing fibers with carbon nanotubes (CNTs) is beneficial for improving the impact properties of ultra-high performance concrete (UHPC); however, the weak wettability and dispersibility of CNTs and the weakly bonded interface between CNTs and UHPC limit their effectiveness as composites. Therefore, this study aims to enhance the reinforcement effect of CNTs on the impact properties of UHPC via functionalization. Unlike ordinary CNTs, functionalized CNTs with carboxyl or hydroxyl groups can break the Si–O–Ca–O–Si coordination bond in the C–S–H gel and form a new network in the UHPC matrix, effectively inhibiting the dislocation slip inside UHPC matrix. Furthermore, functionalized CNTs, particularly carboxyl-functionalized CNTs, control the crystallization process and microscopic morphology of the hydration products, significantly decreasing and even eliminating the width of the aggregate–matrix interface transition zone of the UHPC. Moreover, the functionalized CNTs further decrease the attraction of the negatively charged silicate tetrahedron to Ca^{2+} in the C–S–H gel, while modifying the pore structure (particularly the nanoscale pore structure) of UHPC, leading to the expansion of the intermediate C–S–H layer. The changes in the microstructures of UHPC brought about by the functionalized CNTs significantly enhance its dynamic compressive strength, peak strain, impact toughness, and impact dissipation energy at strain rates of 200–800 s^{-1}. Impact performance of UHPC containing a small amount of carboxyl-functionalized CNTs (especially the short ones) is generally better than that of UHPC containing hydroxyl-functionalized and ordinary CNTs; it is even superior to that of UHPC with a high steel fiber content.

© 2021 THE AUTHORS. Published by Elsevier LTD on behalf of Chinese Academy of Engineering and Higher Education Press Limited Company. This is an open access article under the CC BY-NC-ND license (http://creativecommons.org/licenses/by-nc-nd/4.0/).

1. Introduction

In complex and extreme service environments, static-load-bearing concrete structures may be gradually affected by dynamic loads such as impacts and explosions. Under the action of dynamic impact loads, the large amount of strain energy inside the concrete material leads to a shorter compression time and smaller effective stress area in the material [1], which, in turn, exacerbates the brittle failure of concrete and considerably affects the safety of concrete structures.

Researchers have attempted to design ultra-high performance concrete (UHPC) structures to withstand extreme loads based on the understanding of their dynamics [2–5]. The principle behind using UHPC is that it hinders the propagation path of cracks by improving the compactness of the cement matrix and the bridging effect of fibers, thereby increasing the energy absorption of the concrete material [6–8]. Wang et al. [9] found that the addition of 1%–2% of steel fibers (0.16 mm in diameter and 13 mm in length) effectively reduces the crushing degree of UHPC specimens under impact loads. Wang et al. [10,11] suggested that by incorporating different sizes (0.175–0.200 mm in diameter, 6–13 mm in length) and contents (3%–6%) of steel fiber, the damage softening of UHPC can be improved when the strain rate is between 40 and 100 s^{-1}. Hou et al. [12] reported that at a strain rate of 75–274 s^{-1}, the dynamic elastic modulus and energy absorption of

* Corresponding authors.
E-mail addresses: dongsufen@dlut.edu.cn (S. Dong), hithanbaoguo@163.com (B. Han).

https://doi.org/10.1016/j.eng.2021.04.030
2095-8099/© 2021 THE AUTHORS. Published by Elsevier LTD on behalf of Chinese Academy of Engineering and Higher Education Press Limited Company.
This is an open access article under the CC BY-NC-ND license (http://creativecommons.org/licenses/by-nc-nd/4.0/).

UHPC can be significantly increased by adding 2%–5% of steel fiber. Al-Masoodi et al. [13] also found that W-shaped steel fibers can increase the dynamic compressive strength and energy absorption of concrete by up to 83.3% and 162.2% at strain rates of 30 and 50 s^{-1}, respectively. Tai [14] performed the split Hopkinson pressure bar (SHPB) test on fiber-reinforced UHPC specimens at a strain rate of 10–1000 s^{-1}. They found that both the impact toughness and energy absorption of UHPC increase with an increase in the fiber content (1%–3%) and strain rate. When the strain rate ranges from 500 to 800 s^{-1}, the energy absorption of UHPC with 3% steel fiber increases by up to 175%. Dong et al. [15] also found that at a strain rate of 94–926 s^{-1}, the addition of super-fine stainless wire leads to increase of 33.7%, 43.5%, and 58.2% in dynamic compressive strength, dynamic impact toughness, and impact dissipation energy (IDE) of UHPC, respectively. In summary, researchers have carried out substantial work on the anti-impact properties of UHPC and have achieved substantial results. In fact, the absence of coarse aggregates in UHPC leads to a large number of (fine) aggregate–matrix interfaces inside the composites [2,16,17]. According to the compact packing theory, a lot of fine powders coated with water films will accumulate in the interface area, which weakens the overall performance of the UHPC. However, the problem of multi-interfaces between different compositions in UHPC has not been well studied.

In particular, at strain rates greater than 200 s^{-1}, the weak interface bond between the fibers and the UHPC matrix tends to induce stress concentration points at the interface, which considerably compromises the anti-impact performance of UHPC [18]. Moreover, the incorporation of fibers inevitably leads to new pores forming in the UHPC matrix, which, in turn, affects the shrinkage and durability of the material [19]. Therefore, it has become critical to develop approaches addressing the defects of UHPC while ensuring its high toughness.

In recent years, rapid progress in nanotechnology has led to the development of nanofiller-modified UHPC. The overall properties of UHPC can be considerably changed through nanomodification [20–24]. Among existing nanomaterials, carbon nanotubes (CNTs) with excellent mechanical properties and thermal properties are regarded as ideal nanofillers that can replace traditional fibers in concrete composites [20,25–28]. Compared with traditional fibers, CNTs with a hollow tubular structure can store free water during the early stage of hydration and release it at a later stage, thus promoting the late-age hydration of concrete materials [29]. Furthermore, the high specific area of CNTs enables them to be distributed widely in a material matrix even at low contents, which significantly improves the microstructure of the composite material [30,31]. This means that the incorporation of CNTs can ensure a compact UHPC matrix and further improve the microstructure of UHPC. In this manner, the energy absorption ability of UHPC is increased and the brittleness of the material is effectively reduced. The corresponding experimental results have been reported by Wang et al. [32].

However, as hydrophobic substances, CNTs have weak wettability, which often makes it difficult for them to form good bonds with the matrix material [33–35]. Moreover, the strong interlayer van der Waals between the CNT interlays easily leads to their agglomeration [36], drastically limiting the application of CNTs in UHPC. To completely utilize the superior properties of CNTs, surface modification of CNTs, especially with functional group treatment, has been performed [37]. Studies have shown that functionalized CNTs have significantly enhanced wettability and hydrophilicity, which improves the dispersion of nanotubes in the concrete matrix [38,39]. More importantly, functional groups on the surface of functionalized CNTs can increase the surface activation points of nanotubes and form strong chemical interfacial bonds with the concrete matrix [40,41], thereby improving the composite efficiency and effect of the nanotubes. Theoretically, the incorporation of functionalized CNTs can significantly improve the overall performance of UHPC [42,43], and therefore improve its impact resistance under high strain rates. Unfortunately, research on the anti-impact properties of functionalized CNT-modified UHPC has not been conducted, and the effectiveness of the strengthening mechanism of functionalized CNTs under impact loading is still unknown.

To this end, this study used functionalized CNTs to modify UHPC and investigated its anti-impact properties through an SHPB test. Considering the differences in the nanotube aspect ratio and functional group treatment for crack inhibition, the effects of different types and lengths of functionalized CNTs (including carboxyl- and hydroxyl-functionalized ones) on the anti-impact properties were compared, and the modification mechanisms of UHPC were analyzed across multiple scales—macroscopic, microscopic, and nanoscopic. Finally, the impact compression behavior of UHPC was verified using an established dynamic compression constitutive model. These results are of great significance to the detailed understanding of the dynamic mechanical behavior and reinforcing mechanism of UHPC. Moreover, they have the potential to aid the development of UHPC with high impact resistance.

2. Materials and experiments

2.1. Raw materials and mix proportion

Table 1 lists the raw materials and mix proportions of UHPC with and without CNTs. The types and contents of mineral admixtures were the same for all the types of UHPC. The water-to-cement ratio of UHPC in this study was 0.375, and the corresponding water-to-binder (including cement, fly ash, and silica fume) ratio was 0.24. In addition to a control UHPC (C0), 0.25% and 0.50% of functionalized CNTs by weight of cement were considered for each type of functionalized CNT-modified UHPC. The physical properties of these types of multi-walled CNTs are presented in Table 2. Functionalized CNTs, including those functionalized by hydroxylation (MH) and carboxylation (MC), are synthesized in H_2SO_4 solutions by chemical oxidation ($KMnO_4$) of ordinary CNTs, and functionalized CNTs with short lengths (SMH) are mechanically cut from the respective long CNTs. The effect of ordinary CNTs on the anti-impact properties of UHPC has been reported in another article by the authors [32], which is referred to here when considering the performance of the functionalized CNTs.

In addition, UHPC specimens with dimensions of ϕ30 mm × 15 mm and ϕ20 mm × 40 mm were prepared for the impact compression experiment and pore structure characterization, respectively. Before performing the relevant experiments, all the UHPC specimens were cured in water at 25 °C for 90 days. To reduce the interference of the end-friction effect of the specimen during the impact test, the surfaces of all the specimens were polished to achieve a roughness value within 0.05 mm [44]. The representative data for each type of UHPC are the average of three sets of valid data.

2.2. Experiments

2.2.1. Impact compression test

The impact compression test was performed using an SHPB device. To ensure propagation of the one-dimensional stress wave, the diameter of the impact bar was set to 37.0 mm, and the length-to-slenderness ratio of the pressure bar was adjusted [45]. Three different strain rates (approximately 200, 500, and 800 s^{-1}) were achieved by adjusting the emission pressure (0.125–0.5000 MPa), and the elastic waves in the elastic bars were collected by the

Table 1
Raw materials and mix proportion of UHPC with and without CNTs.

Code	Cement	Fly ash	Silica fume	Sand	Water	Superplasticizer	CNTs					
							OL	OS	MH	SMH	MC	SMC
C0	1	0.25	0.3125	1.375	0.375	1.5%	—	—	—	—	—	—
CL1/CL2	0.9975/ 0.9950	0.25	0.3125	1.375	0.375	1.5%	0.25%/ 0.50%	—	—	—	—	—
CS1/CS2	0.9975/ 0.9950	0.25	0.3125	1.375	0.375	1.5%	—	0.25%/ 0.50%	—	—	—	—
CH1/CH2	0.9975/ 0.9950	0.25	0.3125	1.375	0.375	1.5%	—	—	0.25%/ 0.50%	—	—	—
CSH1/ CSH2	0.9975/ 0.9950	0.25	0.3125	1.375	0.375	1.5%	—	—	—	0.25%/ 0.50%	—	—
CC1/CC2	0.9975/ 0.9950	0.25	0.3125	1.375	0.375	1.5%	—	—	—	—	0.25%/ 0.50%	—
CSC1/ CSC2	0.9975/ 0.9950	0.25	0.3125	1.375	0.375	1.5%	—	—	—	—	—	0.25%/ 0.50%

CL1, CS1, CH1, CSH1, CC1, and CSC1 denote the UHPC containing 0.25% of OL, OS, MH, SMH, MC, and SMC, respectively, while CL2, CS2, CH2, CSH2, CC2, and CSC2 denote UHPC containing 0.50% of OL, OS, MH, SMH, MC and SMC, respectively. Besides, OL denotes ordinary CNTs with a long length. OS denotes ordinary CNTs with a short length. MH and SMH denote hydroxyl-functionalized CNTs with long length and short length, respectively. MC and SMC denote carboxyl-functionalized CNTs with long length and short length, respectively.

Table 2
Physical properties of different types of CNTs.

Types	Purity (%)	Length (μm)	ID (nm)	OD (nm)	SSA ($m^2 \cdot g^{-1}$)	–OH content (wt%)	–COOH content (wt%)
OL	> 98	10–30	2–5	< 8	> 350	—	—
OS	> 98	0.5–2	2–5	< 8	> 350	—	—
MH	> 98	10–30	5	8	> 400	5.58	—
SMH	> 98	0.5–2	5	8	> 380	5.58	—
MC	> 98	10–30	5	8	> 400	—	3.86
SMC	> 98	0.5–2	5	8	> 270	—	3.86

ID denotes inner diameter and OD denotes outer diameter; SSA denotes the specific surface area.

strain gauge. To balance the overall deformation rate of the material while ensuring the validity of the data, the transverse deformation rate before the peak stress was selected as the representative strain rate [10]. The average stress σ, average strain rate ε_s and average strain ε were calculated according to the three-wave method formulas, as follows [46]:

$$\begin{cases} \sigma = \frac{EA_b}{2A_{UHPC}}[\varepsilon_{in} + \varepsilon_{re} + \varepsilon_{tr}] \\ \dot{\varepsilon}_s = \frac{c}{l_{UHPC}}[\varepsilon_{in} - \varepsilon_{re} - \varepsilon_{tr}] \\ \varepsilon(t) = \int_0^t \dot{\varepsilon}_{sr}(\tau)\mathrm{d}\tau \end{cases} . \quad (1)$$

where A_b and A_{UHPC} are the cross-sectional areas of the bar and UHPC specimens, respectively. ε_{in}, ε_{re}, and ε_{tr} are the strains obtained from the incident, reflected, and transmitted pulses, respectively. t and τ are the load duration time parameters. c is the wave speed in the bar, E is the elastic modulus of the bar, and l_{UHPC} is the initial thickness of the UHPC specimens.

2.2.2. Scanning electron microscopy analysis

To further investigate the interaction between CNTs and the cement matrix and to establish clear evidence of the CNT location in the cement matrix, the microscopic morphology of UHPC was analyzed using Nova Nano scanning electron microscope (SEM) 450 machine (FEI Ltd., USA). Prior to SEM observations, all UHPC specimens were cut into dimensions of 1 cm × 1 cm × 0.5 cm and dried at 55 °C for 24 h. Subsequently, a thin gold layer was coated on the surfaces of the specimens using Q150TES (Quorum Ltd., UK).

2.2.3. Pore structure characterization

The pore structure of UHPC was characterized using a LIME-MRI-D2 nuclear magnetic resonance (NMR) rock core analyzer (Beijing Limecho Technology Co., Ltd., China), and the transverse relaxation behavior of ^{1}H protons in water was captured by the Carr–Purcell–Meiboom–Gill (CPMG) pulse sequence. The magnetic rotation ratio of the hydrogen nucleus was 42.58 MHz·T^{-1}, and the magnetic field intensity was (0.3 ± 0.05) T. To capture the relaxation characteristics of water confined in different pores, the echo interval of the CPMG pulse sequence was set to 60 s, and the numbers of collected echoes s to 30 000 and 32, respectively [47].

The UHPC specimens used for pore structure characterization were cylindrical with a diameter of 20 mm and a height of 40 mm. The working principle of low-field NMR (LF-NMR) is based on the "diffusion metamodel" [48,49]. The relationship between the surface relaxation time and pore structure can be expressed as

$$\frac{1}{T_2} = \frac{1}{T_{2BUL}} + \lambda\left(\frac{1}{T_{2SUR}} - \frac{1}{T_{2BUL}}\right)\frac{A_{SUR}}{V_{SPV}} \quad (2)$$

where T_{2SUR} is the relaxation time of the surface water layer, T_{2BUL} is the relaxation time of bulk water, λ is the thickness of the surface liquid layer, V_{SPV} is the specific pore volume, A_{SUR} is the surface area, and T_2 is the relaxation time.

3. Results and analysis of mechanical properties

3.1. Anti-impact properties of functionalized CNT-modified UHPC

3.1.1. Dynamic compressive strength and strain rate effect

Fig. 1 shows the dynamic compressive strength of UHPC containing different types and contents of CNTs. The relationship between the dynamic compressive strength and strain rate of the UHPC is shown in Figs. 2(a)–(c).

It can be observed from Fig. 1 that regardless of whether the functionalized CNTs are incorporated or not, the dynamic compressive strength of UHPC increases as the strain rate increases, indicating a strain rate effect in the UHPC specimens. Similar to

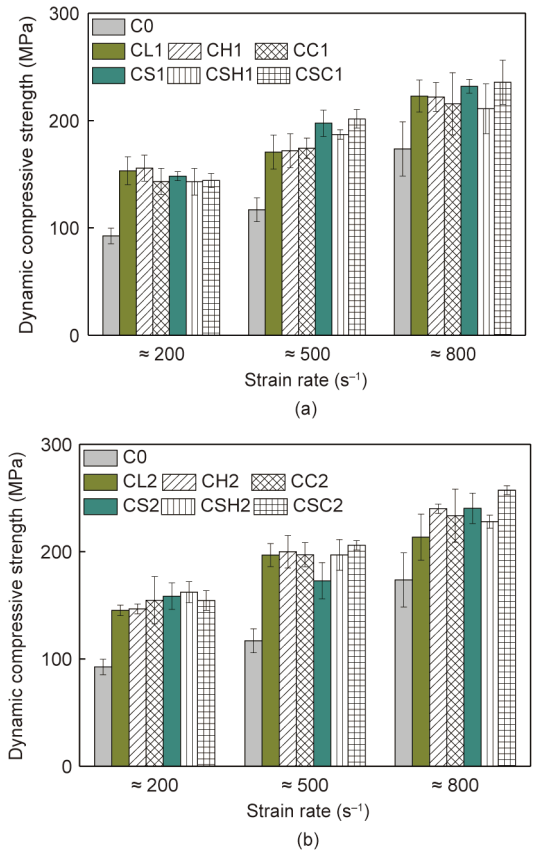

Fig. 1. Dynamic compressive strength of UHPC containing different types and contents of CNTs compared to the control UHPC. (a) UHPC with 0.25% CNTs; (b) UHPC with 0.50% CNTs.

ordinary CNTs (including ordinary CNTs with a long length (OL) and short length (OS)), all types of incorporated functionalized CNTs increase the dynamic compressive strength of UHPC within comparable strain rates. Except for the UHPC modified with hydroxyl-functionalized CNTs at a strain rate of 200 s^{-1} and the UHPC modified with carboxyl-functionalized CNTs at a strain rate of 500 s^{-1}, the dynamic compressive strength of other types of functionalized CNT-modified UHPC significantly increases with increasing CNT content. Specifically, at a CNT content of 0.25% and strain rate of 200–800 s^{-1} (as shown in Fig. 1(a)), the incorporation of the four types of functionalized CNTs (including MH, MC, SMH, and SMC) can increase the dynamic compressive strength of the control UHPC (C0) by 68.2%, 55.2%, 59.9%, and 72.4%, respectively. When the CNT content is 0.50% (as seen in Fig. 1(b)), the corresponding increase in the strength of these four types of UHPC reaches 71.0%, 68.9%, 75.3%, and 76.2%. The dynamic compressive strength of UHPC with added functionalized CNTs is significantly greater than that of UHPC with traditional steel fibers (increase of approximately 10%–50%) [12,14,15]. Interestingly, the dynamic compressive strength of UHPC with 0.25% functionalized CNTs (except for some cases of carboxyl-functionalized CNTs) is close to or slightly lower than that of ordinary CNT-modified UHPC. When the CNT content reaches 0.50%, this phenomenon is reversed, that is, except for hydroxyl- and carboxyl-functionalized CNTs with short lengths, functionalized CNTs are superior to ordinary CNTs in terms of improving the strength of UHPC. Among all types of functionalized CNTs, carboxyl-functionalized CNTs with short length have an obvious advantage in increasing the dynamic compressive strength of UHPC, which is 9.7% higher than that of UHPC with ordinary CNTs.

The increase in the dynamic compressive strength of UHPC at a high strain rate is mainly related to the formation of a large number of microcracks, which requires higher energy consumption than crack propagation [50]. Compared with the control UHPC, the incorporation of CNTs further fills the nanopores and micropores between hydration products [51] and enhances the interface bonding of the cement matrix [29], thereby significantly increasing the energy required for crack formation. It is worth noting that hydroxyl-functionalized CNTs, with increased wettability and enhanced hydrophilic properties, can significantly improve the dispersion of nanotubes, effectively reducing their agglomeration in the UHPC matrix (especially at high CNT contents) [38,39]. Furthermore, the oxygen-containing functional groups on the surface of carboxyl-functionalized CNTs react with calcium hydroxide [40,41]. As a result, more calcium silicate hydrate (C–S–H) gels are formed, and the strength of UHPC is further increased.

It can be observed from Fig. 2 that at CNT contents of 0.25% and 0.50%, the dynamic compressive strength of all UHPC presents a certain linear relationship with the strain rate, which is consistent with the results of UHPC without CNTs, thus demonstrating the strain rate effect of UHPC [52,53]. However, following the incorporation of CNTs, the slope (k) of the strength–strain rate regression curves of most UHPC specimens (except for UHPC containing 0.50% carboxyl-functionalized CNTs) is lower than that of UHPC without CNTs. Specifically, the slope of the strength–strain rate regression curve decreases from 0.13533 to 0.05689, with a maximum decrease of 57.9%. This implies that the incorporation of CNTs weakens the strain rate sensitivity of UHPC [54]. It is worth noting that functionalized CNTs with long lengths present lower slopes than ordinary CNTs with long lengths, but this phenomenon seems to be reversed when short nanotubes are considered.

It is generally believed that the strain rate effect of UHPC is the result of the joint action of the microcrack propagation effect and the inertia effect, which, in turn, increase the energy absorption capacity of UHPC [52,53,55]. With the incorporation of CNTs, the crack tip stress is directed away, via the bridging nanotubes, to the cement matrix, thus delaying crack propagation. Furthermore, the denser network of CNTs causes stress redistribution in the matrix [20,40], which, in turn, offsets the lateral inertial force of the composite material and somewhat suppresses its confining pressure effect. In addition, the functional groups in functionalized CNTs further strengthen the chemical bond between nanotubes and the UHPC matrix [20,41,51] and improve the load transfer of the CNTs to the UHPC matrix [20,29]. These advantages of functionalized CNTs significantly improve the structural uniformity of UHPC, which causes more energy to be consumed in the process of crack development. This is mechanistically different from normal UHPC, which consumes energy simply by increasing the stress. The different strain rate effects of CNTs with various lengths may be related to the fact that different-sized CNTs have different dispersion effects in the concrete matrix. Specifically, CNTs with short lengths have a better dispersion ability than the long ones [56], which improves the network structure of the UHPC matrix and increases the complexity of the stress distribution, thus reducing the confining pressure effect of UHPC.

3.1.2. Dynamic compressive deformation

To further investigate the impact behaviors of the functionalized CNT-modified UHPC, the dynamic stress–strain curves of all UHPC specimens are presented in Figs. 3(a) and (b).

As shown in Figs. 3(a) and (b), the dynamic stress–strain curves of UHPC can be roughly divided into two sections: approximately linear ascending and nonlinear descending sections, corresponding to the elastic–plastic deformation and strain softening of the material, respectively [52,53]. As the strain rate gradually increased, both the dynamic peak stress and limit strain of UHPC increased,

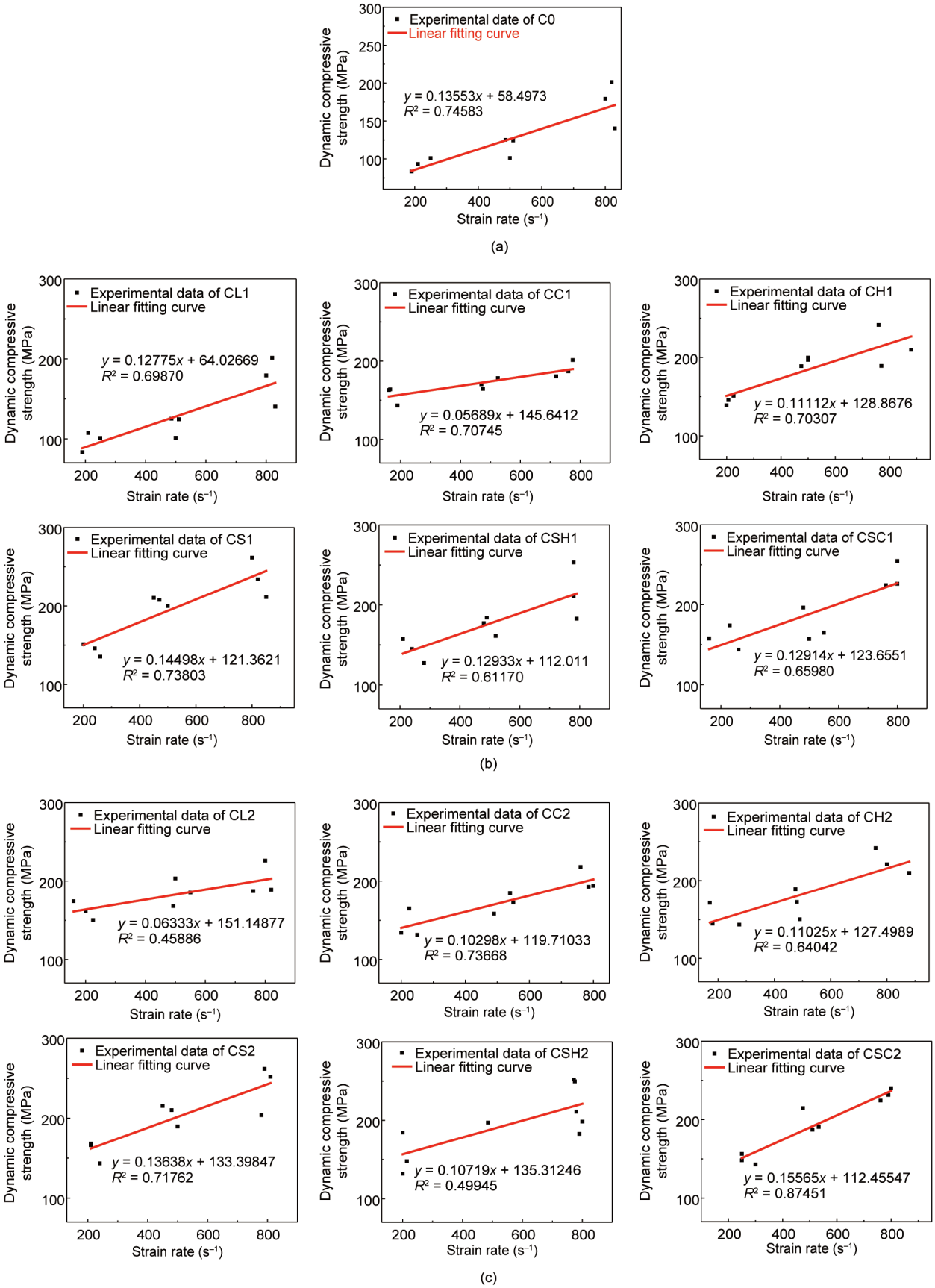

Fig. 2. Relationship between dynamic compressive strength and strain rate of UHPC with different types and contents of CNTs. (a) UHPC without CNTs (control); (b) UHPC with 0.25% CNTs; (c) UHPC with 0.50% CNTs.

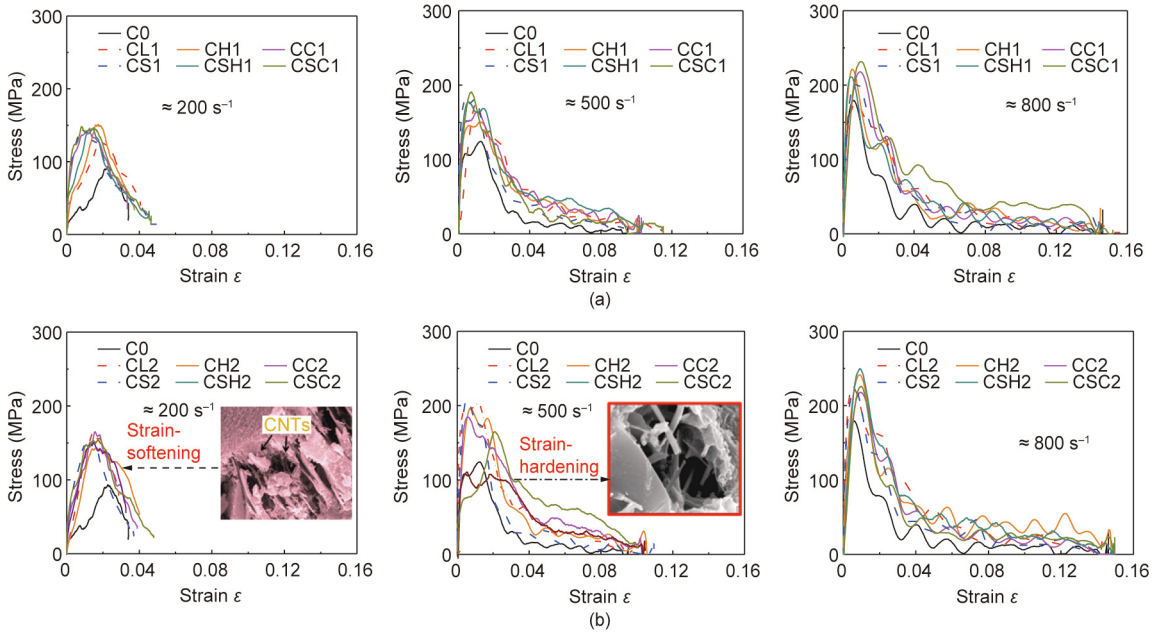

Fig. 3. Dynamic stress–strain curves of UHPC with different types and contents of CNTs. (a) 0.25% CNTs; (b) 0.50% CNTs.

demonstrating the strain rate effect of UHPC. However, the slope of the stress–strain curve of the UHPC significantly increased in the ascending section but gradually slowed down in the descending section owing to the presence of functionalized CNTs. In particular, at a CNT content of 0.50% and strain rate of 500 s^{-1}, the dynamic stress–strain curves of functionalized CNT-modified UHPC exhibit a "sawtooth" shape, indicating the strain-hardening phenomenon [10,11]. This implies that the incorporation of functionalized CNTs not only increases the elastic modulus and residual strength of UHPC, but also causes the damage behavior of UHPC to change from simple matrix cracking to fiber fracture [57].

The bridging and pull-out effects of functionalized CNTs redistribute the stress inside the UHPC matrix and then impede the propagation paths of the cracks, which is particularly critical for improving the impact resistance of UHPC. The corresponding experimental phenomena have also been confirmed in the UHPC matrix by SEM observations, as shown in Fig. 4. It should be noted that compared with ordinary CNTs, functionalized CNTs with oxygen-containing groups increase sp^3 hybridization of the tube walls and enhance the weak interface friction between the nanotubes. In this way, the dislocation density in the UHPC matrix increases, and the dislocation slip is effectively hindered [36–38]. Furthermore, functionalized CNTs with a high surface activity can increase their probability of contact with cement particles, which, in turn, attracts more hydration products to form an intermediate phase [29,40,41]; thus, the fiber effect of CNTs is enhanced.

Figs. 5(a) and (b) show the dynamic peak strain of UHPC containing different CNTs compared with the control UHPC. The cracking form and structure enhancement of the functionalized CNT-modified UHPC are shown in Figs. 5(c) and (d). It can be observed from Figs. 5(a) and (b) that, similar to ordinary CNTs, incorporating functionalized CNTs significantly decreases the dynamic peak strain of UHPC at a strain rate of 200–500 s^{-1}, but makes the strain value of UHPC gradually approach or even exceed that of the control UHPC at high strain rate. What's more, compared with the decreased strain value of ordinary CNTs modified UHPC at high strain rate (up to 30.3%), incorporating functionalized CNTs can increase the strain value by 101.1% (with a difference of 131.4%). This means that functionalized CNTs intensify the dynamic embrittlement of UHPC at medium and low strain rates [58] but delay the unsteady propagation of microcracks at high strain rates (i.e., improve the plastic deformation of the material). It should be noted that with increasing strain rate, the peak strain of a composite material generally increases first and then decreases owing to the provision of traditional fibers [9,12,14,15], which is in contrast

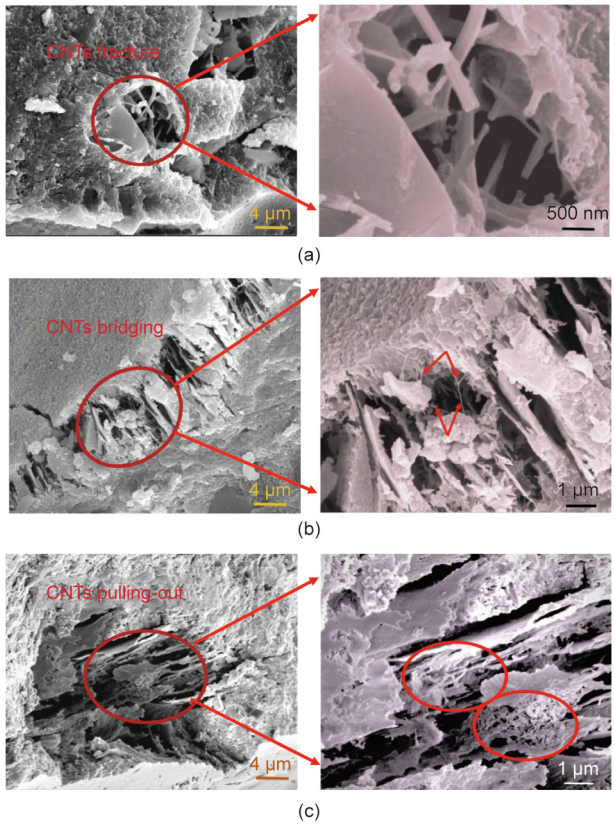

Fig. 4. Different failure modes of functionalized CNTs in UHPC matrix. (a) CNTs fracture; (b) CNTs bridging; (c) CNTs pulling-out.

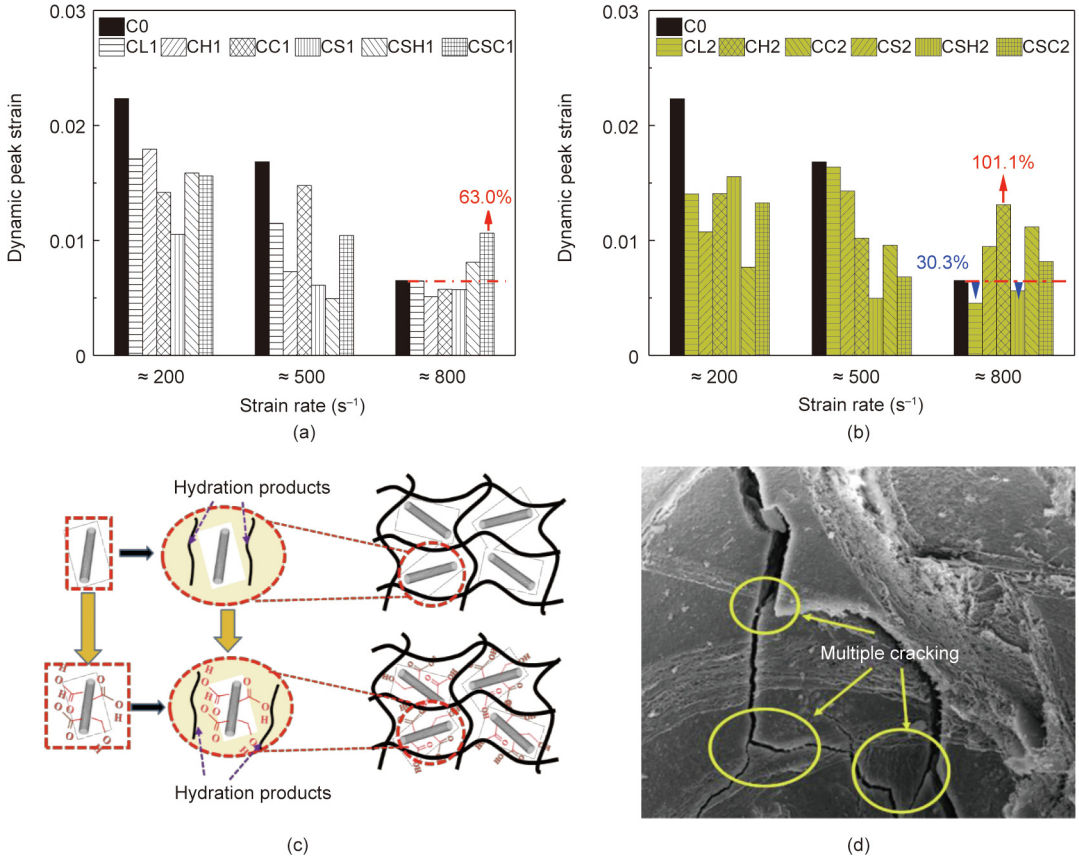

Fig. 5. (a, b) Dynamic peak strain of UHPC; (c) structural integrity of CNT-modified UHPC; (d) multiple cracking inside the hydroxyl-functionalized CNT-modified UHPC matrix.

to the results presented in this paper. This is because compared with traditional fibers, functionalized CNTs further increase the matrix compactness and the interface bonding strength of the UHPC [29,51], thereby improving the composite material's structural integrity. As a result, the material phases are more uniform, and multiple cracking is induced inside the UHPC matrix (c) and (d). However, a large number of microcracks at high strain rates inevitably require the CNTs to induce the fiber-bridging effect, which, in turn, obstructs the propagation path of microcracks and therefore weakens the dynamic embrittlement of UHPC. All the above phenomena show that functionalized CNTs, especially carboxyl-functionalized CNTs, significantly enhance the impact resistance of UHPC.

3.1.3. Dynamic compression toughness

The impact resistance of UHPC mainly depends on its energy consumption before destruction. Therefore, the dynamic impact toughness and IDE were calculated to characterize the anti-impact properties of UHPC, as shown in Fig. 6. The dynamic impact toughness, as a comprehensive measure of the strength and ductility of a material, is obtained by integrating the stress–strain curve [59]. The IDE reflects the energy dissipated by the stress wave during material failure and is calculated according to Eq. (3) [60].

$$\mathrm{IDE} = \frac{AEc}{A_{\mathrm{UHPC}} l_{\mathrm{UHPC}}} \int_0^T \left[\varepsilon_{\mathrm{in}}(t)^2 - \varepsilon_{\mathrm{re}}(t+\tau_1)^2 - \varepsilon_{\mathrm{tr}}(t+\tau_2)^2\right] \mathrm{d}t \tag{3}$$

where T is the time when the UHPC specimen is completely destroyed. τ_1 and τ_2 are time delays of reflected and transmitted pulses, respectively.

Fig. 6 indicates that, within the comparable strain rates, all types of functionalized CNT-modified UHPC show higher dynamic impact toughness and IDE than the control UHPC (C0). This becomes more evident as the CNT content increases. Specifically, in the strain rate range of 200–800 s^{-1}, incorporating hydroxyl-functionalized CNTs increases the impact toughness and IDE of the control UHPC (C0) by 101.6% and 89.0%, respectively, while incorporating carboxyl-functionalized CNTs increases the two toughness indexes of the control UHPC by 106.2% and 94.6%. Compared with ordinary CNTs, functionalized CNTs can further improve the dynamic impact toughness and IDE of UHPC by 5.5% and 16.8%, respectively.

From the perspective of energy dissipation, the initial cracks or small holes in the concrete material could hinder the propagation of the stress wave, causing energy attenuation during the propagation process [61]. Compared with the control UHPC, the incorporation of functionalized CNTs can increase the energy dissipation of the UHPC mainly from two aspects: on the one hand, functionalized CNTs, as viscoelastic materials, exhibit a time delay in their mechanical response, which can transform the kinetic energy caused by impact into strain energy and dissipate it in the form of heat energy [62]. On the other hand, the increased surface activation points of functionalized CNTs enhance the interfacial bond strength between the nanotubes and the cement matrix, thereby increasing the cohesive force of the UHPC [63]. In addition, the interlaminar slip and structural fracture of the functionalized CNTs themselves and the viscous friction between the nanotubes and the UHPC matrix further absorb the strain energy released by matrix cracking, significantly increasing the energy absorption capacity of the UHPC. Eventually, the energy consumption of the material increases, and the stress wave dissipation intensifies.

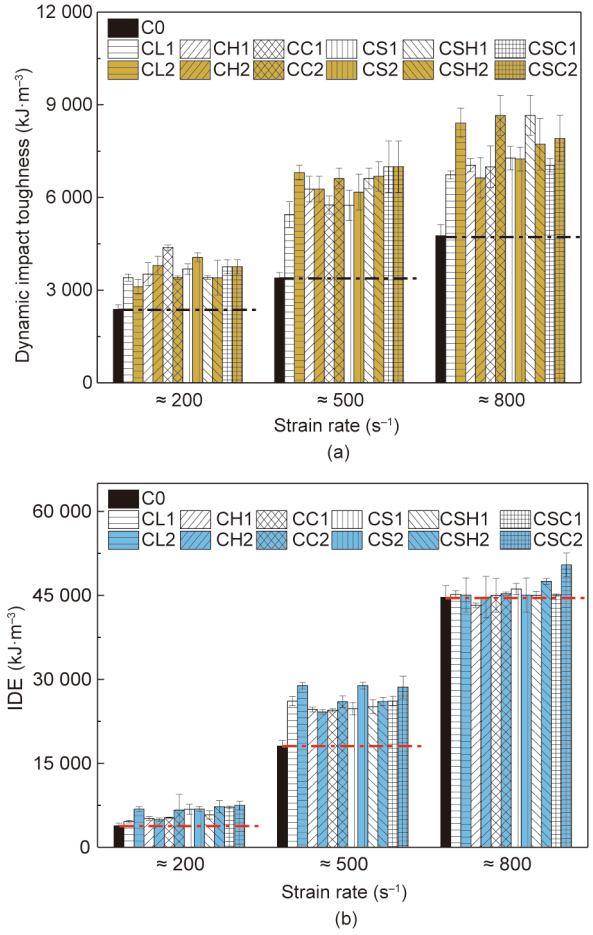

Fig. 6. (a) Impact toughness and (b) IDE of UHPC with different types and contents of CNTs.

3.2. Reinforcing mechanisms of functionalized CNTs

The external properties of concrete composites are determined by the hardened cement paste. The hardened cement paste is primarily influenced by its microstructure, including its pore structure and the physical morphology of hydration products. Studies have found that the destruction of concrete composites mostly involves the gradual development of internal microscopic cracks and defects, which eventually expand to macroscopic cracks [64,65]. If nanoscale cracks can be reduced and the development of microscale cracks can be prevented, the propagation of macroscale cracks can be considerably avoided [66,67]. Therefore, the physical morphology of hydration products was further observed by SEM, and the pore structure of UHPC was characterized using LF-NMR technology. In this way, the microstructure of UHPC was investigated, and the modification mechanism of the functionalized CNTs was determined.

3.2.1. Micromorphology of UHPC

Fig. 7(a) shows the aggregate–matrix interfacial transition zone (ITZ) of UHPC containing different types of CNTs. The corresponding micromorphology of the UHPC matrix is shown in Fig. 7(b).

As shown in Fig. 7(a), UHPC modified with CNTs (including ordinary and functionalized CNTs) has a narrower gap between the aggregate–matrix interface than the control UHPC without CNTs. In particular, when carboxyl-functionalized CNTs are incorporated, the interface gap almost disappears and the hydration products near the ITZ appear in the form of a three-dimensional braided network. This implies that the presence of functionalized CNTs significantly improves the weak area of the UHPC, enhancing the interfacial bonding of the UHPC matrix and increasing the structural integrity of UHPC. As shown in Fig. 7(b), a large number of stacked plate-like calcium hydroxide crystals appear in the control UHPC, and the size of calcium hydroxide crystals is generally greater than 10 μm. However, with the incorporation of CNTs, calcium hydroxide crystals with sizes smaller than 5 μm appear in the UHPC matrix and are distributed randomly. The aforementioned phenomena indicate that CNTs, particularly functionalized CNTs, can control the crystallization process of hydration products and adjust their microscopic morphology. In this manner, the cracks along the fracture path of the crystals inside the UHPC become more tortuous, and the toughness of UHPC is significantly enhanced.

The regulation of hydration products by functionalized CNTs can be explained from two aspects. First, the strong adsorption of functionalized CNTs enables large amounts of free water in the UHPC matrix and ITZ to be absorbed, limiting the growth space of calcium hydroxide crystals and decreasing the orientation degree of calcium hydroxide crystals [40]. Second, functionalized CNTs with high specific surface areas and large aspect ratios can be enriched in the ITZ, firmly bonding the nanotubes to the hydration products and the ITZ [68]. Additionally, for carboxyl-functionalized CNTs, the carboxylate groups on the surface of the nanotubes can bond with Ca^{2+} and decrease the concentration of Ca^{2+} in the C–S–H gel [69,70]. As a result, the Si–O–Ca–O–Si coordination bond in the C–S–H gel structure is broken, and a new network with nanotubes as nodes is formed in the concrete matrix to attract more nanoscale C–S–H gels, as shown in Fig. 8. In this manner, the ITZ width inside the UHPC decreases, and the compactness and network structure of the UHPC matrix are significantly enhanced.

3.2.2. Pore structure characteristics of UHPC

Although it is reasonable to assume that UHPC has a continuous pore size distribution [71], the multi-exponential inversion is widely determined to obtain the discrete components of concrete material [72–75]. According to Mehta and Monteiro [76], pores with different characteristic radii in C–S–H can be classified as interlayer pores (0.22–0.48 nm), gel pores (1.69–2.33 nm), and capillary pores (greater than 2.5 nm). Inner C–S–H pores include interlayer pores and gel pores, while outer C–S–H pores include fine and coarse capillary pores [67,76]. Therefore, this study first derives the continuous pore size distribution of UHPC and then identifies the discrete characteristic pores. In this regard, the pore structure characteristics of the UHPC are quantified, and the modification mechanisms of the functionalized CNTs are fully understood. The experimental results, including the porosity and equivalent pore radius of UHPC, are shown in Figs. 9(a)–(c). The modification mechanisms of functionalized CNTs on the pore structure are shown in Fig. 9(d).

As shown in Fig. 9(a), functionalized CNTs do not significantly change the pore size distribution of UHPC, and the pores are still distributed in the size range of 0.1–10 nm and 10–1000 nm. However, with an increase in the functionalized CNT content, both the porosity and critical pore radius of UHPC remarkably decrease by 5.5%–24.0% and 0–24.2%, respectively. This means that the provision of functionalized CNTs fills the pores inside the UHPC and refines the pore size.

Figs. 9(b) and (c) indicate that, although the presence of functionalized CNTs decreases the inner and outer porosity of C–S–H, resulting in a denser C–S–H gel, it also causes significant fluctuations in the sizes of different characteristic pores inside the C–S–H. Specifically, the equivalent radii of both the interlayer and gel pores of C–S–H decrease due to the presence of ordinary CNTs,

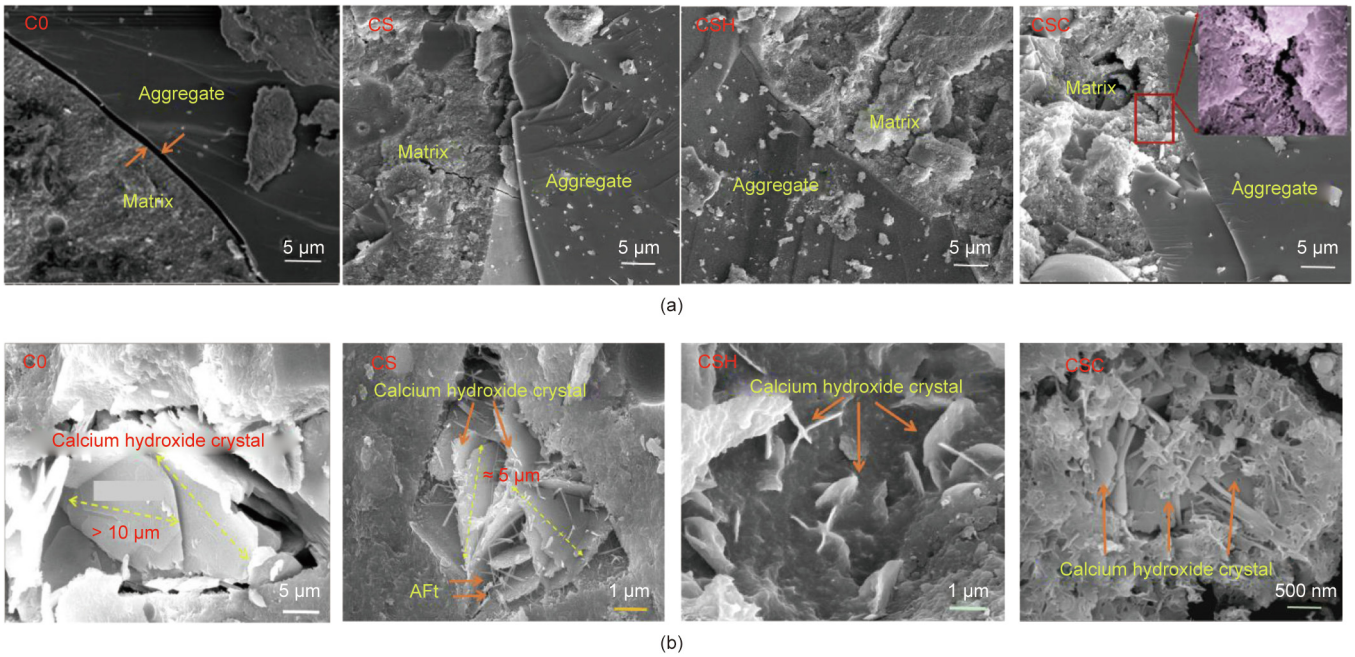

Fig. 7. Micromorphology of UHPC containing different types of CNTs compared to the control UHPC. (a) Improvement of ITZ between aggregate and matrix; (b) limited calcium hydroxide's size and orientation (AFt represents the ettringite).

but this phenomenon gradually reverses with the provision of functionalized CNTs, particularly the short ones. This means that the CNTs do not simply fill and refine the pores, but more importantly, they change the microstructure of hydration products by inducing local contraction or expansion of C–S–H. Ordinary CNTs tend to induce structural shrinkage of the C–S–H gel, while functionalized CNTs tend to expand the interlayer spacing of the gel structure. These small structural changes in the C–S–H gel significantly affect the macroscopic properties of UHPC.

The improved pore structure of UHPC results from the formation and deposition of hydration products [77], which can be achieved by the nucleation effect of CNTs [20,29,30,40]. It should be noted that CNTs with a small size and high specific surface area can absorb the surface water of the C–S–H and increase the interaction force between the pore wall and water molecules inside the C–S–H layers. Consequently, the C–S–H layers surrounding the pore water become compact, and structural shrinkage of the C–S–H gel occurs [78]. Unlike ordinary CNTs, functionalized CNTs, particularly carboxyl-functionalized CNTs, can further reduce the attraction of the negatively charged silicate tetrahedron $[SiO_4]^{4-}$ to Ca^{2+} in the intermediate layer of C–S–H through absorption of Ca^{2+}. As a result, the absorbed Ca^{2+} forms a new silicon chain with the silica tetrahedron, resulting in the expansion of the intermediate C–S–H layer. The corresponding mechanism has been reported in the literature [79,80]. In addition, an increase in the negative pore water pressure causes the functionalized CNTs (especially the short ones) to release their own stored water. In this process, the interlayer pores and gel pores with a larger specific surface area first absorb moisture, and the disjointing pressure of water drives the contacting C–S–H layers to separate and expand again [81,82].

3.3. Dynamic damage constitutive model

3.3.1. Model formulation

Studies have shown that concrete materials have viscoelastic hysteresis and strain rate characteristics under dynamic impact loading. To reflect the dynamic stress–strain behavior of concrete accurately, the ZWT model was selected in this study, as expressed in Eq. (4) [60]. The ZWT model is a typically nonlinear-viscoelastic dynamic constitutive model. It is based on the elastic model and considers the viscous effect, which is consistent with the dynamic mechanical behavior of concrete materials in this work [60,83].

$$\sigma = f_e(\varepsilon) + E_1 \int_0^t \dot{\varepsilon} \exp\left(-\frac{t-\tau}{\theta_1}\right) + E_2 \int_0^t \dot{\varepsilon} \exp\left(-\frac{t-\tau}{\theta_2}\right) \mathrm{d}\tau \tag{4}$$

where $f_e(\varepsilon)$ represents the stress–strain behavior of the nonlinear spring and is expressed as $f_e(\varepsilon) = E_0\varepsilon + \mu\varepsilon^2 + \eta\varepsilon^3$; E_0, μ, and η are the elastic constants; E_1 and E_2 represent the elastic modulus of the low-frequency and high-frequency Maxwell elements, and θ_1 and θ_2 are the relaxation times of these two Maxwell elements [60].

Considering the transiency of the loading process (10^{-6}–10^{-3} s loading time) and the small deformation of concrete materials, the ZWT model can be simplified to Eq. (5).

$$\sigma = E_0 + E_2 \int_0^t \varepsilon \exp\left(-\frac{t-\tau}{\theta_2}\right) \mathrm{d}\tau \tag{5}$$

where the relaxation time of the low-frequency Maxwell element is ignored and the nonlinear rising section of the stress–strain curve is simplified to linear rising [83].

It is known that the damage development of concrete-like materials is essentially attributed to the initiation, propagation, and mutual penetration of cracks. To reflect the material damage with the increase in stress/strain, the damage factor is introduced into the dynamic compression model as shown in Eq. (6) [84]. Considering that the damage factor satisfies the two-parameter Weibull statistical distribution [85] as expressed in Eq. (7), the simplified ZWT model is finally revised to Eq. (8).

$$\sigma_m = \sigma(1-D) + Dk \tag{6}$$

$$D = \begin{cases} 0 & \varepsilon \le \varepsilon_{th} \\ 1 - e^{-\left(\frac{\varepsilon - \varepsilon_{th}}{m}\right)^{\alpha}} & \varepsilon \ge \varepsilon_{th} \end{cases} \tag{7}$$

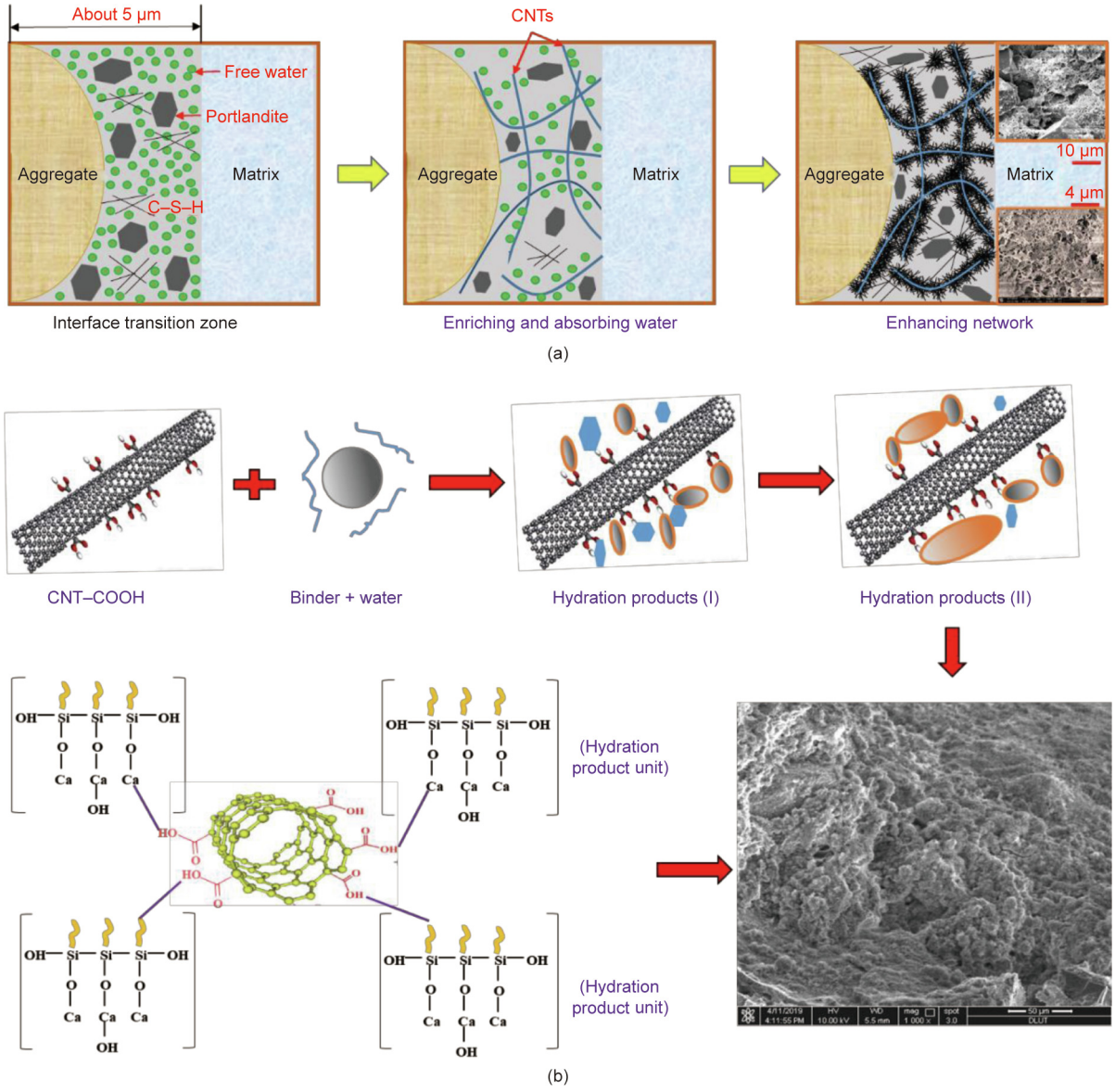

Fig. 8. (a) Enrichment effect and (b) network enhancement of functionalized CNTs on the ITZ of UHPC.

$$\sigma_m = \begin{cases} E_0\varepsilon + E_2\theta_2\dot{\varepsilon}\left[1 - \mathrm{e}^{-\varepsilon/(\theta_2\dot{\varepsilon})}\right] \\ \mathrm{e}^{-\left(\frac{(\varepsilon-\varepsilon_{\mathrm{th}})}{m}\right)^{\alpha}}\left\{E_0\varepsilon + E_2\theta_2\dot{\varepsilon}\left[1 - \mathrm{e}^{-\varepsilon/(\theta_2\dot{\varepsilon})}\right]\right\} + \left[1 - \mathrm{e}^{-\left(\frac{(\varepsilon-\varepsilon_{\mathrm{th}})}{m}\right)^{\alpha}}\right]k \end{cases} \tag{8}$$

where m, k, and α are the damage parameters, which are determined by the matrix strength and the functionalized CNT content. $\varepsilon_{\mathrm{th}}$ is the strain threshold, which is 70% of the peak strain.

3.3.2. Verification of model

The comparison between the experimental and fitting results of the dynamic compression constitutive model of the functionalized CNT-modified UHPC is shown in Fig. 10. The corresponding fitting parameters of the constitutive UHPC model are listed in Table 3. As shown in Fig. 10, during the entire dynamic compression loading process, the fitting results of the dynamic damage constitutive model of UHPC were in good agreement with the experimental results. Overall, the initial elastic modulus of the functionalized CNT-modified UHPC is higher than that of the control UHPC, and the damage parameters of UHPC vary with the change in strain rate. Therefore, the constitutive model presented in this study can effectively characterize the dynamic compression behavior of functionalized CNT-modified UHPC, which conforms to the viscoelastic properties of the material and has a damage mechanism similar to that of fiber-reinforced concrete.

4. Conclusions

In this study, the anti-impact properties of UHPC reinforced with different types and lengths of functionalized CNTs (including carboxyl-functionalized and hydroxyl-functionalized CNTs) were characterized using the SHPB test. Further, the hydration product morphology and pore structure characteristics of functionalized CNT-modified UHPC were analyzed using SEM and LF-NMR technologies. Eventually, the modification mechanisms of functionalized CNTs on UHPC were revealed, and the dynamic mechanical behaviors of UHPC were verified by the established dynamic damage constitutive model. The conclusions are as follows:

(1) Under the strain rate range of 200–800 s^{-1} and CNT content of 0.25%–0.50%, all the types of incorporated functionalized CNTs

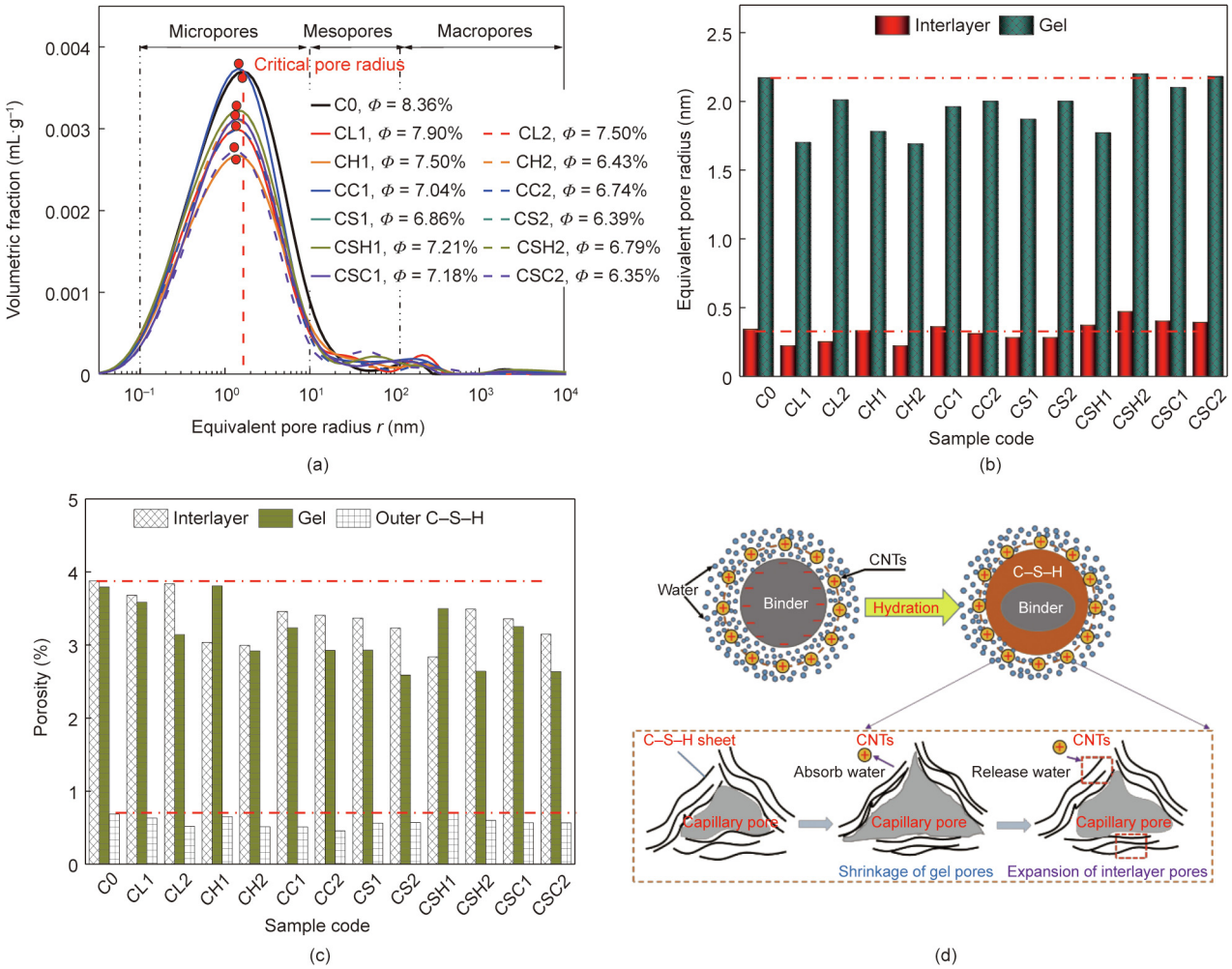

Fig. 9. (a)–(c) Pore structure characteristics of UHPC, and (d) modification mechanisms of functionalized CNTs-modified UHPC. Φ is the symbol for porosity.

significantly enhance the anti-impact properties of UHPC. Specifically, the fiber bridging and network enhancement of functionalized CNTs reduce the crack propagation and confining pressure effect of the UHPC, resulting in a decrease in the strain rate sensitivity. The bridging, fracture, and pull-out of functionalized CNTs change the damage mechanism of UHPC from simple matrix cracking to fiber breakage, significantly improving the energy absorption ability of UHPC.

(2) Among all the types of functionalized CNTs, carboxyl-functionalized CNTs, especially the short ones, significantly improve the anti-impact performance of UHPC. This is closely related to the higher surface activity and better dispersibility of the nanotubes, which promote cement hydration and improve the matrix network structure. Overall, the dynamic compressive strength and peak strain of UHPC can be increased by 9.7% and 131.4%, respectively, owing to the presence of functionalized CNTs, while the increase in impact toughness and IDE of UHPC reaches 5.5% and 16.8%, respectively, with respect to UHPC with ordinary CNTs.

(3) SEM observations show that the incorporation of functionalized CNTs can control the crystallization process of hydration products and adjust their physical morphology, which improves the ITZ of the aggregate matrix and also enhances the network structure of the UHPC matrix. LF-NMR characterization shows that functionalized CNTs reduce the porosity and pore size of UHPC; meanwhile, they induce structural contraction or expansion of C–S–H by changing the surface water content of the C–S–H. The strong absorption of Ca^{2+} by carboxyl-functionalized CNTs changes the C–S–H gel structure in a better way than hydroxyl-functionalized CNTs and ordinary CNTs. In this manner, the cracks along the fracture path inside the UHPC become more tortuous, and the toughness of UHPC is significantly enhanced.

(4) Functionalized CNTs, especially the short ones, are superior to ordinary CNTs in improving the anti-impact properties of UHPC and can approach or even exceed the improvement in impact performance of concrete brought by high steel fiber content. This is closely related to their high hydrophilicity, high wettability, and strong interfacial bond. In this way, the dispersion of functionalized CNTs inside the UHPC matrix is improved, and the composite efficiency and effect between the nanotubes and the material matrix are increased.

(5) The fitting results of the established dynamic damage constitutive model are highly consistent with the experimental results, indicating that the proposed constitutive model can effectively represent the dynamic compressive mechanical properties of functionalized CNT-modified UHPC. This implies that the mechanical behavior of this type of concrete material still satisfies the viscoelastic mechanics and statistical damage theory.

The chemical bonding and physical junction between the functionalized CNTs and UHPC matrix together with the effect of functionalized CNTs on the microstructure of hydration products significantly enhance the anti-impact properties of UHPC. The

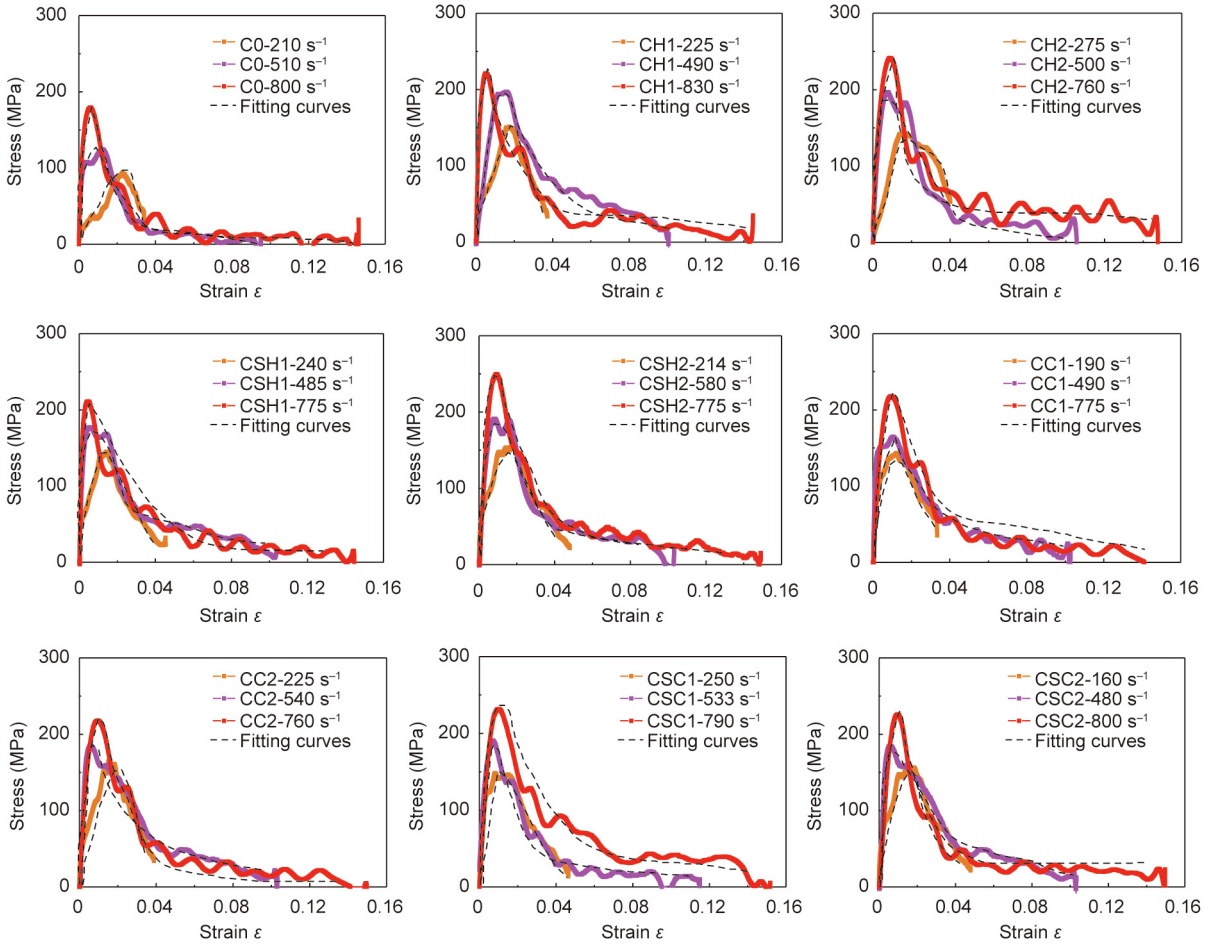

Fig. 10. Experimental and fitted stress–strain curves of UHPC with different types and contents of CNTs.

Table 3
Fitting parameters of ZWT model.

Code	Strain rate (s^{-1})	ε_{th} ($\times 10^{-3}$)	E_0 (GPa)	E_2 (GPa)	θ_2 (μs)	m ($\times 10^{-3}$)	α	k
C0	210	15.9	2.46	35.85	2.13	16.15	6.54	19.98
	510	8.5	5.63	10.42	2.11	18.51	2.68	8.94
	800	4.3	20.07	24.87	8.89	36.20	0.72	47.06
CH1	225	11.4	10.22	0.24	0.61	13.32	1.81	28.90
	490	5.8	3.62	36.57	2.25	43.61	1.85	49.61
	830	3.7	57.55	22.72	7.68	44.33	0.85	18.74
CH2	275	10.4	8.18	2.16	0.86	20.51	2.06	25.39
	500	5.1	25.78	15.68	6.14	13.83	0.50	63.47
	760	6.4	26.63	17.65	0.24	23.32	0.66	13.62
CSH1	240	10.1	7.63	9.80	2.02	80.31	0.36	14.84
	485	3.7	25.17	31.18	2.71	32.85	0.99	7.75
	775	3.3	30.57	38.76	3.33	67.12	2.10	49.56
CSH2	214	9.2	10.14	4.61	0.39	20.77	2.01	38.17
	580	4.4	17.86	22.14	2.32	60.01	3.04	46.16
	780	6.4	17.56	21.75	3.01	47.51	2.02	53.96
CC1	190	8.7	9.09	11.25	0.36	12.95	2.72	54.49
	490	7.5	14.12	17.49	0.18	49.71	2.11	56.67
	775	6.4	15.78	19.54	1.41	64.00	4.16	38.46
CC2	225	9.0	6.31	8.83	0.48	19.85	4.51	43.63
	540	3.9	20.41	25.28	0.93	13.71	1.03	40.15
	760	6.6	15.61	19.33	1.09	45.75	1.94	52.07
CSC1	250	5.7	13.63	16.88	0.31	14.41	1.54	44.76
	533	4.9	19.87	24.60	3.92	3.90	1.14	43.12
	790	7.1	15.69	9.44	0.17	11.09	3.15	67.56
CSC2	160	7.6	10.67	13.21	0.56	10.36	0.52	16.30
	480	3.0	8.24	10.20	3.39	46.81	0.78	53.39
	800	2.0	35.06	43.15	1.79	55.13	2.35	63.18

results of this study provide a theoretical basis for the application of UHPC in special structures.

Acknowledgments

The authors would like to thank the National Natural Science Foundation of China (51978127 and 51908103), the Fundamental Research Funds for the Central Universities (DUT21RC(3)039), and the China Scholarship Council Foundation (202006060103) for providing funding to carry out this investigation.

Compliance with ethics guidelines

Jialiang Wang, Sufen Dong, Sze Dai Pang, Xun Yu, Baoguo Han, and Jinping Ou declare that they have no conflict of interest or financial conflicts to disclose.

References

[1] Forrestal MJ, Wright TW, Chen W. The effect of radial inertia on brittle samples during the split Hopkinson pressure bar test. Int J Eng Sci 2007;34(3):405–11.
[2] Richard P. A new ultra-high strength cementitious material. In: Proceedings of 4th International Symposium on Utilization of High Strength/High Performance Concrete. 1996 May 29–31; Paris, France. Paris: Presses Ponts et Chaussees. p. 1343–9.
[3] Doroud K, Moshaii A, Pezeshkian Y, Rahighi J, Afarideh H. Simulation of temperature dependence of RPC operation. Nucl Instrum Methods Phys Res Sect A 2009;602(3):723–6.
[4] Lee M, Wang GYC, Chiu CA. Preliminary study of reactive powder concrete as a new repair material. Constr Build Mater 2007;21(1):182–9.
[5] Dong YR, Xu ZD, Xu YS, Waseem S, Li QQ. Seismic performance and multi-scale model of damage evolution for reinforced concrete frame structures. ACI Struct 2021;118(2):3–15.
[6] Ma HY, Tang SW, Li ZJ. New pore structure assessment methods for cement paste. J Mater Civ Eng 2015;27(2):A4014002.
[7] Rouquerol J, Avnir D, Fairbridge CW, Everett DH, Haynes JM, Pernicone N, et al. Recommendations for the characterization of porous solids. Pure Appl Chem 1994;66(8):1739–58.
[8] Dong SF, Wang YY, Ashour A, Han BG, Ou JP. Uniaxial compressive fatigue behavior of ultra-high performance concrete reinforced with super-fine stainless wires. Int J Fatigue 2021;142:105959.
[9] Wang YH, Wang ZD, Liang XY, An MZ. Experimental and numerical studies on dynamic compressive behavior of reactive powder concretes. Acta Mech Solida Sin 2008;21(5):420–30.
[10] Wang Z, Liu Y, Shen RF. Stress-strain relationship of steel fiber-reinforced concrete under dynamic compression. Constr Build Mater 2008;22(5):811–9.
[11] Wang Z, Shi Z, Wang J. On the strength and toughness properties of SFRC under static–dynamic compression. Compos B Eng 2011;42(5):1285–90.
[12] Hou X, Cao S, Rong Q, Zheng W, Li G. Effects of steel fiber and strain rate on the dynamic compressive stress-strain relationship in reactive powder concrete. Constr Build Mater 2018;170:570–81.
[13] Al-Masoodi AHH, Kawan A, Kasmuri M, Hamid R, Khan M. Static and dynamic properties of concrete with different types and shapes of fibrous reinforcement. Constr Build Mater 2016;104:247–62.
[14] Tai YS. Uniaxial compression tests at various loading rates for reactive powder concrete. Theor Appl Fract Mech 2009;52(1):14–21.
[15] Dong S, Han B, Yu X, Ou J. Dynamic impact behaviors and constitutive model of super-fine stainless wire reinforced reactive powder concrete. Constr Build Mater 2018;184:602–16.
[16] Hu J, Stroeven P. Properties of the interfacial transition zone in model concrete. Interface Sci 2004;12(4):389–97.
[17] Scrivener KL, Crumbie AK, Laugesen P. The interfacial transition zone (ITZ) between cement paste and aggregate in concrete. Interface Sci 2004;12(4):411–21.
[18] Buitelaar P. Ultra-high performance concrete: developments and applications during 25 years. In: Proceedings of the 1st International Symposium on Ultra-High Performance Concrete; 2004 Sep 13–15; Kassel, Germany.
[19] Li VC, Leung CKY. Theory of steady state and multiple cracking of random discontinuous fiber reinforced brittle matrix composites. J Eng Mech 1992;118(11):2246–64.
[20] Han B, Ding S, Wang J, Ou J. Nano-engineered cementitious composites: principles and practices. Singapore: Springer Singapore; 2019.
[21] Wang J, Dong S, Zhou C, Ashour A, Han B. Investigating pore structure of nano-engineered concrete with low-field nuclear magnetic resonance. J Mater Sci 2021;56(1):243–59.
[22] Wang J, Dong S, Wang D, Yu X, Han B, Ou J. Enhanced impact properties of concrete modified with nanofiller inclusions. J Mater Civ Eng 2019;31(5):04019030.
[23] Wang XY, Dong SF, Li ZM, Han BG, Ou JP. Nanomechanical characteristics of interfacial transition zone in nano-engineered concrete. Engineering 2022;17:99–109.
[24] Wang J, Ding S, Han B, Ni Y, Ou J. Self-healing properties of reactive powder concrete with nanofillers. Smart Mater Struct 2018;27(11):115033.
[25] Yakobson BI, Brabec CJ, Bernholc J. Nanomechanics of carbon tubes: instabilities beyond linear response. Phys Rev Lett 1996;76(14):2511–4.
[26] Treacy MMJ, Ebbesen TW, Gibson JM. Exceptionally high Young's modulus observed for individual carbon nanotubes. Nature 1996;381(6584):678–80.
[27] Wang XY, Zheng QF, Dong SF, Ashour A, Han BG. Interfacial characteristics of nano-engineered concrete composites. Constr Build Mater 2020;259:119803.
[28] Montazeri A, Javadpour J, Khavandi A, Tcharkhtchi A, Mohajeri A. Mechanical properties of multi-walled carbon nanotube/epoxy composites. Mater Des 2010;31(9):4202–8.
[29] Nochaiya T, Chaipanich A. Behavior of multi-walled carbon nanotubes on the porosity and microstructure of cement-based materials. Appl Surf Sci 2011;257(6):1941–5.
[30] Han BG, Sun SW, Ding SQ, Zhang LQ, Yu X, Ou JP. Review of nanocarbon-engineered multifunctional cementitious composites. Compos Part A 2015;70:69–81.
[31] Makar JM, Chan GW. Growth of cement hydration products on single walled multi-walled carbon nanotubes. J Am Ceram Soc 2009;92(6):1303–10.
[32] Wang J, Dong S, Ashraf A, Wang X, Han B. Dynamic mechanical properties of cementitious composites with carbon nanotubes. Mater Today Commun 2020;22:100722.
[33] Zou B, Chen SJ, Korayem AH, Collins F, Wang CM, Duan WH. Effect of ultrasonication energy on engineering properties of carbon nanotube reinforced cement pastes. Carbon 2015;85:212–20.
[34] Mallakpour S, Soltanian S. Surface functionalization of carbon nanotubes: fabrication and applications. RSC Adv 2016;6(111):109916–35.
[35] Andrews R, Weisenberger MC. Carbon nanotube polymer composites. Curr Opin Solid State Mater Sci 2004;8(1):31–7.
[36] Liu J, Zubiri MR, Vigolo B, Dossot M, Fort Y, Ehrhardt J. Efficient microwave-assisted radical functionalization of single-wall carbon nanotubes. Constr Build Mater 2006;45(4):885–91.
[37] Tasis D, Tagmatarchis N, Bianco A, Prato M. Chemistry of carbon nanotubes. Chem Rev 2006;106(3):1105–36.
[38] Li LX, Li F. The effect of carbonyl, carboxyl and hydroxyl groups on the capacitance of carbon nanotubes. N Carbon Mater 2011;26(3):224–8.
[39] Oda H, Yamashita A, Minoura S, Okamoto M, Morimoto T. Modification of the oxygen-containing functional group on activated carbon fiber in electrodes of an electric double-layer capacitor. J Power Sources 2006;158(2):1510–6.
[40] Cui X, Han B, Zheng Q, Yu X, Dong S, Zhang L, et al. Mechanical properties and reinforcing mechanisms of cementitious composites with different types of multiwalled carbon. Compos Part A 2017;103:131–47.
[41] Cwirzen A, Habermehl-Cwirzen K, Penttala V. Surface decoration of carbon nanotubes and mechanical properties of cement/carbon nanotube composites. Adv Cement Res 2008;20(2):65–73.
[42] Andrews R, Jacques D, Minot M, Rantell T. Fabrication of carbon multiwall nanotube/polymer composites by shear mixing. Macromol Mater Eng 2002;287(6):395–403.
[43] Meng L, Fu C, Lu Q. Advanced technology for functionalization of carbon nanotubes. Prog Nat Sci 2009;19:801–10.
[44] Fu Q, Xie Y, Long G, Niu D, Song H, Liu X. Impact characterization and modelling of cement and asphalt mortar based on SHPB experiments. Int J Impact Eng 2017;106:44–52.
[45] Li QM, Meng H. About the dynamic strength enhancement of concrete-like materials in a split Hopkinson pressure bar test. Int J Solids Struct 2003;40(2):343–60.
[46] Miao Y, Li Y, Liu H, Deng Q, Shen L, Mai YW, et al. Determination of dynamic elastic modulus of polymeric materials using vertical split Hopkinson pressure bar. Int J Mech Sci 2016;108–109:188–96.
[47] Liu Z, Liu D, Cai Y, Yao Y, Pan Z, Zhou Y. Application of nuclear magnetic resonance (NMR) in coalbed methane and shale reservoirs: a review. Int J Coal Geol 2020;218:103261.
[48] Muller ACA, Scrivener KL, Gajewicz AM, McDonald PJ. Densification of C-S–H measured by 1H NMR relaxometry. J Phys Chem C 2013;117(1):403–12.
[49] Brownstein KR, Tarr CE. Spin-lattice relaxation in a system governed by diffusion. J Magn Reson 1977;26(1):17–24.
[50] Li G, Gao B. Effect of level SiO_2 and level $CaCO_3$ on concrete performance. J Chin Rai Soc 2006;28(2):131–6. Chinese.
[51] Konsta-Gdoutos MS, Metaxa ZS, Shah SP. Highly dispersed carbon nanotube reinforced cement based materials. Cement Concr Res 2010;40(7):1052–9.
[52] Xiao J, Li L, Shen L, Poon C. Compressive behavior of recycled aggregate concrete under impact loading. Cement Concr Res 2015;71:46–55.
[53] Lai J, Sun W. Dynamic behavior and visco-elastic damage model of ultra-high performance cementitious composite. Cement Concr Res 2009;39(11):1044–51.
[54] Kaplan SA. Factors affecting the relationship between rate of loading and measured compressive strength of concrete. Mag Concr Res 1980;32(111):79–88.
[55] Bischoff P, Perry S. Compressive behavior of concrete at high strain rates. Mater Struct 1991;24(6):425–50.
[56] Manzur T, Yazdani N, Emon MAB. Effect of carbon nanotube size on compressive strengths of nanotube reinforced cementitious composites. J Mater 2014;2014(1):1–8.
[57] Zhu J, Xu J, Bai E, Luo X, Gao Y. Effects of composite nanomaterials on dynamic mechanical properties of concrete. Acta Mater Compos Sin 2016;33(3):597–605. Chinese.

[58] Wu X, Hu S, Chen D, Yu Z. Experimental study on impact compression of steel fiber high strength concrete. Explos Shock Waves 2005;25(2):125–31. Chinese.
[59] Zhang XX, Yu RC, Ruiz G, Tarifa M, Camara MA. Effect of loading rate on crack velocities in HSC. Int J Impact Eng 2010;37(4):359–70.
[60] Lu G, Yu TY. Energy absorption of structures and materials. New Delhi: Woodhead Publishing; 2003.
[61] Jiao C, Sun W. Impact resistance of reactive powder concrete. J Wuhan Univ Technol Mater Sci Ed 2015;30(4):752–7.
[62] Liew KM, Kai MF, Zhang LW. Mechanical and damping properties of CNT-reinforced cementitious composites. Compos Struct 2017;160:81–8.
[63] Arai S, Endo M. Carbon nanofiber-copper composites powder prepared by electrodeposition. Electrochem Commun 2003;5(9):797–9.
[64] Constantinides G, Ulm FJ. The effect of two types of C–S–H on the elasticity of cement-based materials: results from nanoindentation and micromechanical modeling. Cement Concr Res 2004;34(1):67–80.
[65] Tong T, Fan Z, Liu Q, Wang S, Tan S, Yu Q. Investigation of the effects of graphene and graphene oxide nanoplatelets on the micro- and macro-properties of cementitious materials. Constr Build Mater 2016;106:102–14.
[66] McDonald PJ, Rodin V, Valori A. Characterization of intra- and inter-C–S–H gel pore water in white cement based on an analysis of NMR signal amplitudes as a function of water content. Cement Concr Res 2010;40(12):1656–63.
[67] Aligizaki KK. Pore structure of cement-based materials. London; New York: Routledge; 2005.
[68] Wang X, Dong S, Ashour A, Zhang W, Han B. Effect and mechanisms of nanomaterials on interface between aggregates and cement mortars. Constr Build Mater 2020;240:117942.
[69] Lota JS, Pratt PL, Bensted J. Microstructural and micro-analytical studies of sulfate attack. II. sulfate-resisting Portland cement Ferrite composition and hydration chemistry. Cement Concr Res 1995;25(7):18114813.
[70] Plank J, Sachsenhauser B. Experimental determination of the effective anionic charge density of polycarboxylate superplasticizers in cement pore solution. Cement Concr Res 2009;39(1):1–5.
[71] Dunn KJ, Bergman DJ, Latorraca GA. Nuclear magnetic resonance, petrophysical and logging application. Oxford: Pergamon Press Ltd.; 2002.
[72] Bede A, Scurtu A, Ardelean I. NMR relaxation of molecules confined inside the cement paste pores under partially saturated conditions. Cement Concr Res 2016;89:56–62.
[73] Plassais A, Pomiès MP, Lequeux N, Korb JP, Petit D, Barberon F, et al. Microstructure evolution of hydrated cement pastes. Phys Rev E Stat Nonlin Soft Matter Phys 2005;72(4):041401.
[74] Holly R, Reardon EJ, Hansson CM, Peemoeller H. Proton spin–spin relaxation study of the effect of temperature on white cement hydration. J Am Ceram Soc 2007;90(2):570–7.
[75] Muller ACA, Scrivener KL, Gajewicz AM, McDonald PJ. Use of bench-top NMR to measure the density, composition and desorption isotherm of C–S–H in cement paste. Micropor Mesopor Mat 2013;178:99–103.
[76] Mehta PK, Monteiro PJM. Concrete: microstructure, properties, and materials. London: Mc Graw-Hill; 2006.
[77] Maruyama I, Igarashi G, Nishioka Y. Bimodal behavior of C-S–H interpreted from short-term length change and water vapor sorption isotherms of hardened cement paste. Cement Concr Res 2015;73:158–68.
[78] Jennings HM, Bullard JW, Thomas JJ, Andrade JE, Chen JJ, Scherer GW. Characterization and modeling of pores and surfaces in cement paste: correlations to processing and properties. J Adv Concr Technol 2008;6(1):5–29.
[79] Han B, Zhang L, Zeng S, Dong S, Yu X, Yang R, et al. Nano-core effect in nano-engineered cementitious composites. Compos Part A 2017;95:100–9.
[80] Wang J, Han B, Li Z, Yu X, Dong X. Effect investigation of nanofillers on CSH gel structure with Si NMR. J Mater Civ Eng 2019;31(1):04018352.
[81] Persson B. Consequence of cement constituents, mix composition and curing conditions for self-desiccation in concrete. Mater Struct 2000;33(6):352–62.
[82] Dullien FAL. Porous media: fluid transport and pore structure. Cambridge: Academic Press; 1992.
[83] Wang L. Foundation of stress waves. Beijing: National Defense Industry Press; 2010. Chinese.
[84] Løland LE. Continuum damage model for load response estimation of concrete. Cement Concr Res 1980;10(3):395–402.
[85] Hu S, Wang D. Dynamic constitutive relation of concrete materials under impact loading. Explos Shock Waves 2002;22(3):242–6. Chinese.